Journal of Materials Chemistry A

ROYAL SOCIETY OF CHEMISTRY

PAPER

View Article Online
View Journal | View Issue

Cite this: J. Mater. Chem. A, 2024, 12, 1753

Enhanced piezoelectricity and spectral absorption in Nd-doped bismuth titanate hierarchical microspheres for efficient piezo-photocatalytic H_2 production and pollutant degradation†

Yan Zhao, Yan Zhang, * Qianqian Xu, Hanyu Gong, Mingyang Yan, Kaiyu Feng, Xiang Zhou, Xuefan Zhou* and Dou Zhang

Hydrothermally synthesized Nd-doped bismuth titanate ($Bi_{3.15}Nd_{0.85}Ti_3O_{12}$, BIT-Nd) hierarchical microspheres with assembled nanosheets were developed for water splitting and wastewater purification utilizing the piezo-phototronic effect for the first time. Undoped $Bi_4Ti_3O_{12}$ (BIT) microspheres were simultaneously studied for comparison to reveal the role of Nd doping. Under the combined light and ultrasound excitation, the degradation efficiency of RhB (C_0 = 10 mg L^{-1}) solution reached 97.5% in 8 minutes in the presence of the BIT-Nd microspheres, leading to an ultrahigh first-order rate constant k of 0.407 min^{-1}, which was 4.9 times higher than that of the BIT microspheres. More impressively, superior piezo-photocatalytic activity in water splitting compared to that of other reported piezo-photocatalysts was achieved in the BIT-Nd microspheres, which showed a H_2 evolution rate of 1330.3 μmol g^{-1} h^{-1} without any cocatalyst or scavenger. To understand the origins of the excellent piezo-photocatalytic performance, microstructure analysis and piezoelectric and photoelectric characterization, as well as density functional theory calculations were carried out. After Nd doping, the atomic framework of the Ti–O octahedron underwent an apparent distortion, resulting in a stronger ferroelectric polarization, and thus a larger piezoelectric potential output under pressure. Moreover, the thinner nanosheets in the BIT-Nd microspheres were more susceptible to deformation under the ultrasonic effect, which was also beneficial to generate a higher piezoelectric field that inhibited the charge carrier recombination. Additionally, the presence of Nd 4f orbitals in BIT-Nd effectively reduced the band gap and promoted the spectral absorption and production of photogenerated carriers. These merits enabled the BIT-Nd microspheres to exhibit strong piezo-photocatalytic activity.

Received 18th October 2023
Accepted 8th December 2023

DOI: 10.1039/d3ta06341k

rsc.li/materials-a

1. Introduction

The utilization of semiconductor photocatalysts has great potential to alleviate the energy crisis and environmental pollution.[1,2] In general, efficient absorption of light, rapid separation and transfer of photoexcited charge carriers, and abundant active sites contribute to high photocatalytic performance.[3] However, the unsatisfactory solar energy utilization and the high recombination of photoexcited charge carriers in conventional semiconductor materials are significant issues that limit the photoelectric conversion efficiency, and result in weak and inefficient photocatalytic activities. A series of measures to improve the photocatalytic efficiency have been considered which include system innovation,[4] morphology maneuvering,[5] doping modification,[6] and heterostructure construction.[7] Typically, the piezo-phototronic effect in piezoelectric semiconductors with the coupling of the piezoelectric effect and photoelectric effect has been widely studied due to the alternating built-in electric field which is beneficial to facilitate the charge separation.[8–10]

In recent years, the material family showing the piezo-phototronic effect has been extended from metal oxides, *e.g.* ZnO[11] and perovskite structure ferroelectrics, *e.g.* $BaTiO_3$ (ref. 12) to layered two-dimensional (2D) materials, *e.g.* g-C_3N_4.[13] Among the piezo-phototronic semiconductors, bismuth layer-structured ferroelectric $Bi_4Ti_3O_{12}$ (BIT) is particularly attractive owing to its special electronic structure of a hybridized valence band composed of Bi 6s and O 2p orbitals that facilitate the generation of electron–hole pairs,[14] and the favorable ferroelectricty with a spontaneous polarization of ~40 μC cm^{-2} along the a-axis and ~4 μC cm^{-2} along the c-axis.[15] Moreover, the layered structure with $[Bi_2O_2]^{2+}$ bismuth oxide layers and $[Bi_2Ti_3O_{10}]^{2-}$ perovskite layers stacked alternately along the c-

State Key Laboratory of Powder Metallurgy, Central South University, Changsha, Hunan 410000, China. E-mail: zhouxuefan@csu.edu.cn; yanzhangcsu@csu.edu.cn

† Electronic supplementary information (ESI) available. See DOI: https://doi.org/10.1039/d3ta06341k

axis allows the growth of BIT crystals with a 2D shape, which is easy to be deformed under mechanical vibrations.[16] Most of the studies about the piezo-photocatalytic performance of BIT nanostructures are concentrated on wastewater purification, including dye degradation. For examples, Tang *et al.* reported the piezo-photocatalytic activity of BIT nanosheets with different oxygen vacancy concentrations, which reached a $k \sim 0.214\ min^{-1}$ for the decomposition of RhB solution ($C_0 = 5$ mg L^{-1}).[17] Bai *et al.* prepared $Bi_4Ti_{3-2n}Cr_nNb_nO_{12}/x$-g-$C_3N_4$ heterojunctions which showed a piezo-photocatalytic degradation efficiency of RhB ($C_0 = 10$ mg L^{-1}) of 98.7% within 45 min.[18] Nevertheless, the relatively large band gap ($E_g = 3.29$ eV) of BIT limits the spectrum utilization efficiency,[19] and on the basis of the present research, the piezo-photocatalytic performance of BIT-based nanostructures is worth further optimization.

Metal ion doping is a popular and effective strategy to modulate the piezoelectric and photoelectric properties of BIT-based crystals. Rare earth metal ion doping in BIT, *i.e.*, $Bi_{3.25}M_{0.75}Ti_3O_{12}$ (BMT, M = La, Sm, Nd, and Eu), has been proven to be effective to enhance the visible light absorption (narrowed band gap) and restrict the recombination of electron/hole pairs, leading to the improved photocatalytic activity.[20] However, the underlying mechanisms related to the band structure or electronic configuration have not been clarified. On the other hand, in BIT-based bulk ceramics, it has been demonstrated that the substitution of Bi^{3+} by the lanthanide series Nd^{3+} ions with a smaller ionic radius [$r(Bi^{3+}) = 1.30$ Å, $r(Nd^{3+}) = 1.27$ Å] can apparently enhance the spontaneous polarization and thus piezoelectric response due to the increased structural distortion that is the rotation of the TiO_6 octahedron in the *a–b* plane and the incline of the distorted TiO_6 octahedron away from the *c*-axis.[21] For example, Chon *et al.* concluded that the largest value of remanent polarization ($2P_r = 103\ \mu C\ cm^{-2}$) was achieved at $x = 0.85$ in the $Bi_{4-x}Nd_xTi_3O_{12}$ system,[22,23] and the piezoelectric coefficient increased from $\sim$7.3 pC N^{-1} (ref. 24) to $\sim$14 pC N^{-1}.[25] These results inspire us to explore the piezo-photocatalytic performance of Nd-doped BIT nanostructures, which are expected to possess higher piezoelectric potential output and enhanced spectral absorption compared to the widely-studied BIT piezo-phototronic nanocatalysts. Specifically, their piezo-photocatalytic activity in water splitting would be of great interest considering that no relevant research has been conducted to date.

Since the catalytic activity of piezo-photocatalysts is structure-dependent, their morphology design is of significance for efficient light and mechanical energy capture and transformation.[26] One-dimensional nanostructures such as nanowires and nanorods, as well as two-dimensional nanostructures like nanosheets, are inherently inclined towards improving charge separation and reducing charge recombination.[3] Among them, the large flat size of nanosheets provides them with a large capture area for light and mechanical energy, presenting great potential for highly efficient piezo-photocatalysis.[27] In this work, $Bi_{3.15}Nd_{0.85}Ti_3O_{12}$ (BIT-Nd) hierarchical microspheres with assembled nanosheets are synthesized by a hydrothermal method, and we provided the first evaluation of the piezo-photocatalytic performance of the BIT-Nd hierarchical microspheres in the aspects of water splitting for H_2 production and dye degradation at high/low frequencies. Using a combination of piezoresponse force microscopic measurements, UV-vis absorbance spectrum characterization, finite element analysis, and density functional theory calculations, an in-depth understanding of the excellent piezo-photocatalytic performance of the BIT-Nd hierarchical microspheres is presented in this work.

2. Results and discussion

2.1 Morphology and microstructure

Fig. 1(a) shows the XRD patterns of the $Bi_4Ti_3O_{12}$ (BIT) and $Bi_{3.15}Nd_{0.85}Ti_3O_{12}$ (BIT-Nd) powders in the 2θ range of 10–60°. The XRD peaks are well matched with those of orthorhombic $Bi_4Ti_3O_{12}$ (JCPDS #80-2143), demonstrating that Nd^{3+} has been successfully dispersed into the crystal lattice to form a solid solution. The Nd^{3+} ions replace and occupy the Bi^{3+} ion positions due to their similar ionic radii ($r(Nd^{3+}) = 1.27$ Å, $r(Bi^{3+}) = 1.30$ Å). Fig. 1(b) shows that the peak (117) shifts to lower angles with the introduction of Nd, indicating a slight increase in both lattice parameters and volume of the unit cell.[28] In addition, for the pure BIT powders, a typical orthorhombic symmetry was observed, as evidenced by the splitting of $\left(11\underline{15}\right)$ and (202) characteristic peaks at 2θ values of 47.3° and 47.9°, respectively. For BIT-Nd powders, the peak splitting disappeared and only a single peak can be observed, indicating a phase transformation from the orthorhombic phase into the pseudo-cubic structure phase.[29] Fig. 1(c)–(f) show the SEM and AFM images of the BIT and BIT-Nd powders. BIT-Nd exhibits regular spherical structures composed of self-assembled nanosheets with a uniform size. This nanosheet-assembled hierarchical microsphere structure inherits the initial undoped BIT structure. The average edge length of BIT nanosheets is $\sim$470 nm, with an average thickness of $\sim$78 nm. In contrast, the BIT-Nd nanosheets show an edge length of $\sim$400 nm with an average thickness of $\sim$35 nm, which is lower than half of that of the BIT nanosheets. The thinner nanosheets in BIT-Nd reveal that Nd^{3+} doping as intercalation ions in BIT can reduce the crystallization rate of the nanosheets.[30] The EDS mapping reveals a homogeneous distribution of Bi, Ti, Nd and O elements in both BIT and BIT-Nd, as shown in Fig. S1.† Fig. S2† shows that the dominant pore sizes of BIT-Nd and BIT both are $\sim$40 nm, and the surface areas of BET are 32.61 $m^2\ g^{-1}$ and 27.67 $m^2\ g^{-1}$ respectively.

Fig. 1(g)–(i) display the TEM observation results of the BIT-Nd hierarchical microspheres. Fig. 1(g) shows that the assembled nanosheets are well-defined with a clear rectangular outline. The atomic-resolution TEM image, as depicted in Fig. 1(h), exhibits uniform fringes across the entire nanosheet. The interplanar crystal spacings were measured to be 0.265 nm and 0.192 nm, which are in good agreement with the (200) and (220) atomic planes, respectively. The corresponding selected-area electron diffraction (SAED) pattern in Fig. 1(i) shows that BIT-Nd shows a single crystal characteristic. The survey XPS spectra in Fig. 1(j) reveal signals for Bi, Ti, O, Nd, and C

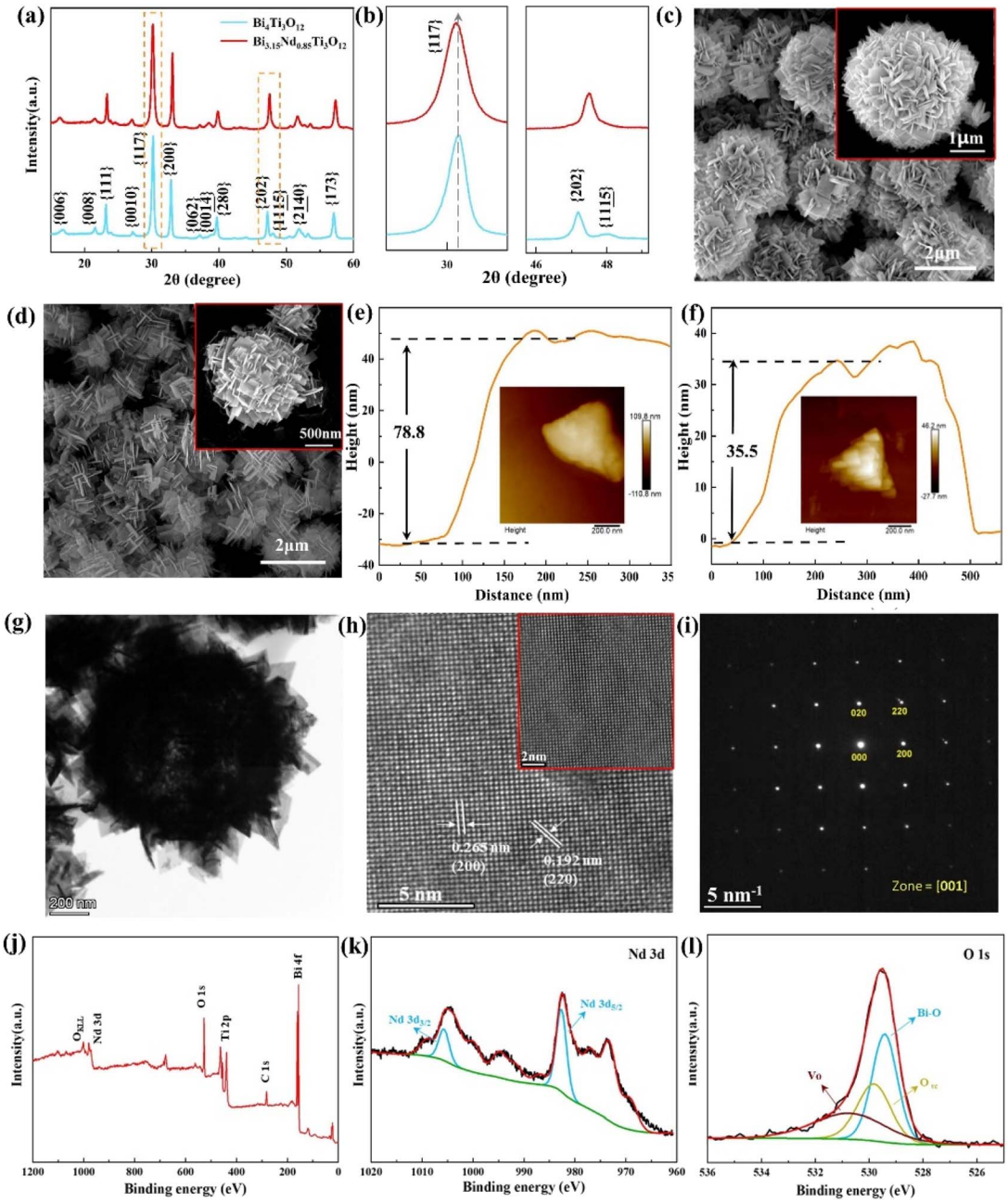

Fig. 1 Morphology and microstructure characterization of the BIT and BIT-Nd hierarchical microspheres. (a) XRD patterns and (b) expanded XRD patterns of the BIT and BIT-Nd powders. SEM images of the (c) BIT and (d) BIT-Nd hierarchical microspheres. AFM images and the corresponding height curves of the (e) BIT nanosheets and (f) the BIT-Nd nanosheets. (g) Bright-field TEM image, (h) atomic-resolution TEM image, (i) SAED pattern, and (j) survey XPS spectrum of the BIT-Nd hierarchical microspheres. High-resolution XPS spectra of (k) Nd 3d and (l) O 1s of the BIT-Nd hierarchical microspheres.

elements, indicating the absence of impurities in BIT-Nd. Based on the value of binding energy, the Bi^{3+} and Ti^{4+} states can be demonstrated as shown in Fig. S3.† Moreover, the XPS spectrum of the Nd 3d peak can be deconvoluted into two peaks at 1005.8 and 982.5 eV by Gaussian processing, as shown in Fig. 1(k), corresponding to Nd $3d_{3/2}$ and Nd $3d_{5/2}$ of Nd^{3+}. Notably, the binding energy located at 531 eV is observed, often attributed to the O_2^- ions in oxygen deficient (V_O) regions (Fig. 1(l)). The presence of V_O favors the adsorption and activation of O_2 molecules on the surface of piezoelectric materials, which is conducive to accumulation of electrons from the localized electrons of oxygen vacancies, ultimately leading to the generation of $\cdot O_2^-$.[31,32]

2.2 Piezoelectric properties and optical properties

The optical responses of the BIT and BIT-Nd hierarchical microspheres were investigated by measuring the UV-vis absorbance spectra as shown in Fig. 2(a). The BIT-Nd

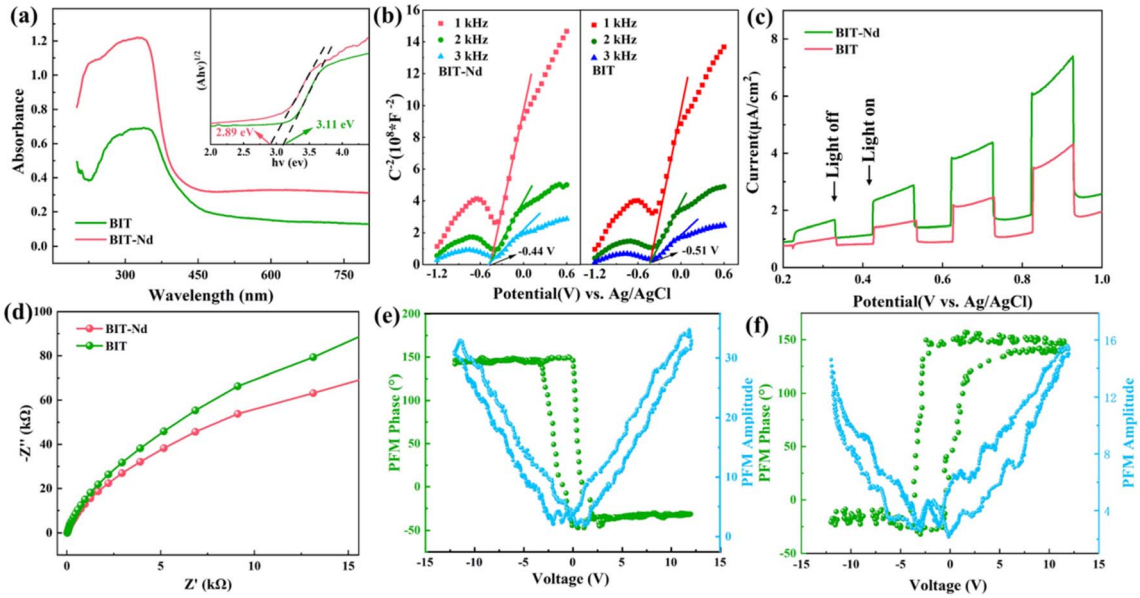

Fig. 2 Piezoelectric and optical properties of the BIT and BIT-Nd hierarchical microspheres. (a) UV-vis diffuse reflectance spectra and the corresponding band gap of BIT and BIT-Nd. (b) Mott–Schottky plots of BIT-Nd and BIT at different frequencies of 1 kHz, 2 kHz, and 3 kHz. (c) Transient photocurrent responses and (d) EIS Nyquist plots of BIT and BIT-Nd. PFM amplitude-voltage butterfly loop and PFM phase hysteresis loop of (e) BIT-Nd and (f) BIT.

powders demonstrated higher absorption intensity in the wavelength range of 450–800 nm, compared with BIT powders, which indicated that the effective doping improved the light absorption performance. Based on the equation of $\alpha hv = B(hv - E_g)^{1/2}$,[33] the band gap ($E_g$) of BIT-Nd and BIT were calculated to be 2.89 eV and 3.11 eV, respectively. Enhanced light absorption and a narrowed band gap are both beneficial to the higher sunlight energy utilization and enhancement of photocatalytic activity. Both BIT and BIT-Nd are n-type semiconductors with positive slopes at different frequencies (1 kHz, 2 kHz, and 3 kHz), as shown in Fig. 2(b). The flat band potential of BIT and BIT-Nd is −0.51 V and −0.44 V, respectively. The transient photocurrent intensities were measured over several cycles of intermittent light irradiation to demonstrate the photo-excited carrier separation behavior of BIT and BIT-Nd, as shown in Fig. 2(c). The photocurrent density of BIT-Nd reaches 7.44 μA cm^{-2} and is 1.7 times higher than that of BIT, indicating that photogenerated carriers are efficiently separated in BIT-Nd. The EIS Nyquist plot of BIT-Nd presents a smaller radius compared to that of BIT, demonstrating the lower charge transport resistance, which contributes to the improvement of piezophotocatalytic activity, as shown in Fig. 2(d). As shown in Fig. 2(e) and (f), by applying a ±12 V DC bias field, both BIT and BIT-Nd exhibit classical amplitude-voltage butterfly loops and well-defined 180° phase reversal hysteresis loops, confirming the existence of ferroelectric switch behavior and piezoelectricity.[34] Importantly, the maximum piezoelectric response amplitude of BIT-Nd is about 2.3 times larger than that of BIT, indicating the higher piezoelectric response of BIT-Nd.[35] Therefore, the BIT-Nd hierarchical microspheres with high surface area, a smaller band gap, stronger photonic excitation, faster charge transfer and higher piezoelectricity could lead to a superior piezo-photocatalytic activity.

To better understand the change in E_g, the theoretical calculations were performed using DFT to investigate the band structures of BIT before and after Nd^{3+} doping. The calculations were based on the BIT unit cell, with consideration given to Nd doping by replacing two Bi atoms with two Nd atoms. As shown in Fig. 3(a) and (b), the calculated E_g of BIT-Nd (1.57 eV) is smaller than that of BIT (2.32 eV), which is consistent with the results of the experimental analysis (Fig. 2(a)). However, both of them are lower than the values of experimental E_g due to the ignored self-interaction correction and discontinuity in the exchange–correlation energy and potential.[36,37] The bottom conduction band (CB) of BIT is mainly composed of Ti 3d and Bi 6p orbitals, whereas the top valence band (VB) is mainly composed of Ti 3d, Bi 6s and O 2p orbitals. The CB of BIT-Nd is mainly attributable to the Ti 3d, Bi 6p and Nd 4f orbitals, and the Ti 3d, Bi 6s and O 2p and Nd 4f orbitals are the main contributions to the VB. The reduction in E_g of BIT-Nd may be attributed to the presence of Nd 4f orbitals and the introduction of an additional spin polarization valence band (SPVB) in the original band gap of BIT.[18]

The influence of Nd^{3+} doping on the ferroelectric polarization was calculated by using DFT, where BIT-Nd was constructed by replacing two Bi atoms in the pseudo-perovskite layer with Nd atoms.[18] Fig. 3(c) and (d) show the structural changes in the Ti–O octahedron in BIT before and after Nd^{3+} doping. Clearly, after substituting Bi with a Nd atom, the atomic framework of the Ti–O octahedron exhibits significant distortion, leading to a reduction in the symmetry of the crystal structure, as shown in Fig. S4.† The Ti–O bond lengths of BIT-Nd decrease, and the [TiO_6] octahedron exhibits a greater

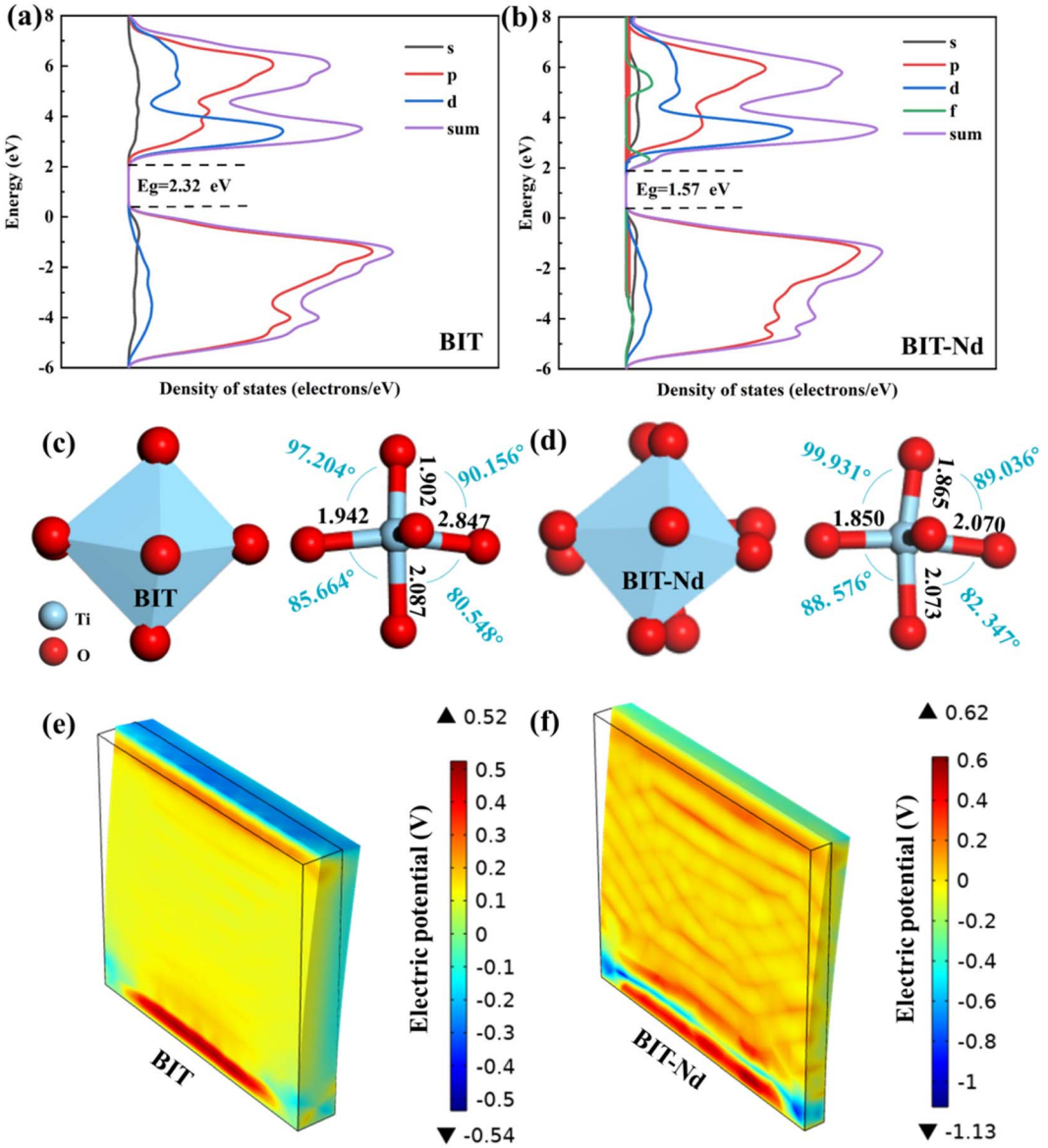

Fig. 3 Theoretical calculations of the band structure and lattice structure of BIT and BIT-Nd. Density of states (DOS) of (a) BIT and (b) BIT-Nd calculated by DFT calculations. [TiO_6] octahedron structures of (c) BIT and (d) BIT-Nd and the corresponding theoretical bond lengths (unit: Å) and bond angles. FEM simulation of the piezoelectric potential distribution in (e) BIT and (f) BIT-Nd nanosheets with lateral deformation.

rotation angle compared to that of BIT. Therefore, for BIT-Nd, the TiO_6 octahedron possesses a larger distortion, which serves to enhance polarization and promote piezoelectric response. To investigate the generated piezoelectric potential distribution in BIT and BIT-Nd nanosheets, finite-element method (FEM) simulations were performed, as presented in Fig. 3(e) and (f). The geometrical parameters, including the edge length and thickness, were close to the actual sizes observed by SEM, as shown in Fig. 1(c) and (d). The size of the simulated BIT was 470 nm × 470 nm × 78 nm, while the size of the simulated BIT-Nd was 400 nm × 400 nm × 35 nm. In addition, the applied stress was set as 100 MPa considering the impact force caused by acoustic cavitation and acoustic pressure[38] and the bottom surface was fixed and grounded.[34] FEM simulation shows that the maximum piezoelectric potential generated by BIT and BIT-Nd nanosheets was 1.06 V and 1.75 V, respectively. The thinner nanosheet has a larger aspect ratio (length/diameter) and a smaller ground contact area than the thicker one, resulting in easier deformation and a higher piezoelectric potential, which may result in a more efficient catalytic process.

2.3 Catalytic activities for dye degradation and H_2 evolution

Fig. 4(a) and (b) illustrate the degradation efficiency of RhB solution in the presence of the BIT-Nd hierarchical microspheres under different degradation conditions. As shown in Fig. 4(a), the degradation of RhB was negligible only under stirring at a speed of 200 rpm (referred to as "stir200 + dark" in Fig. 4), suggesting that low-frequency stirring had little effect on the photocatalytic reaction. However, RhB degradation rates of

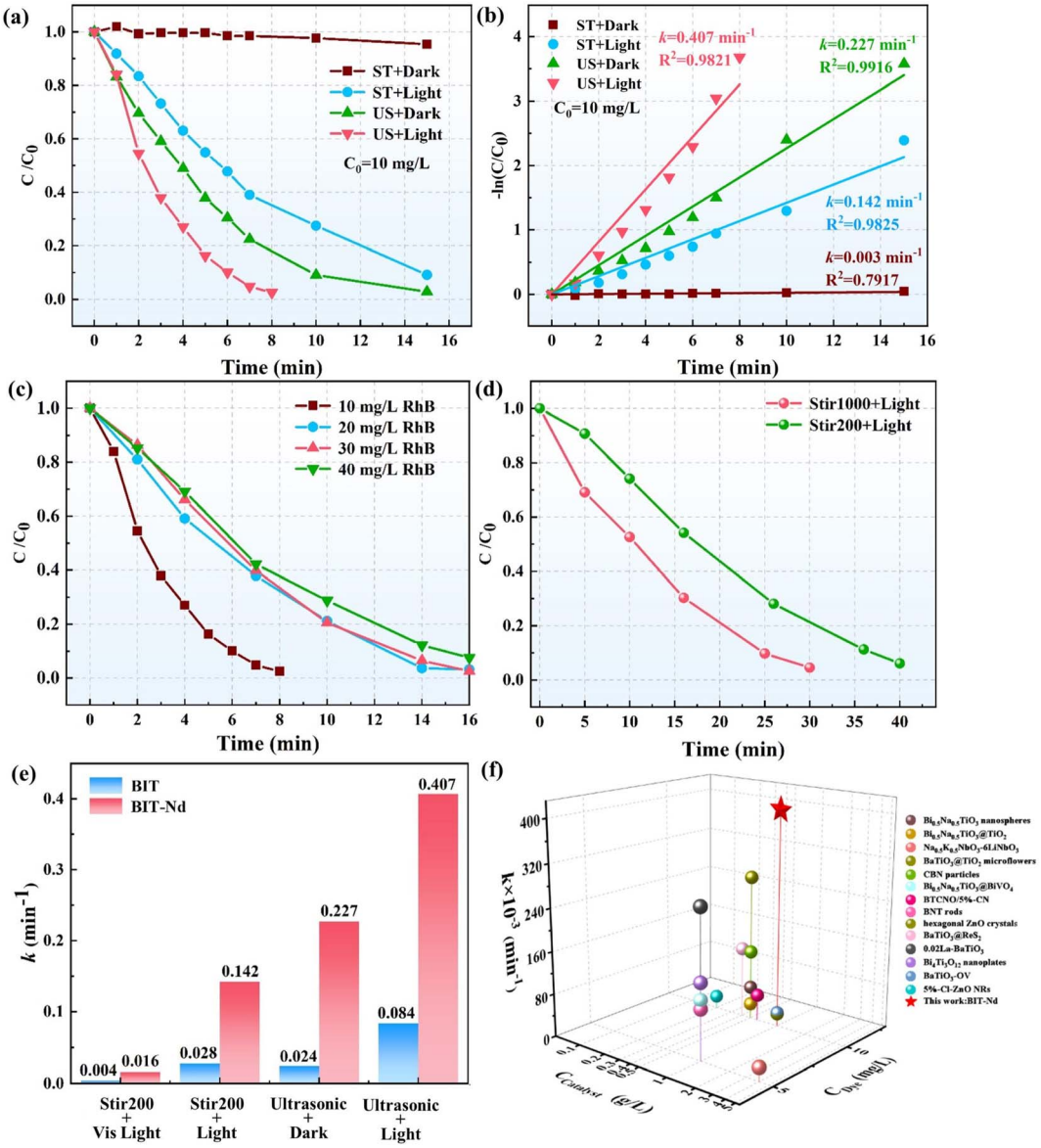

Fig. 4 Piezo-photocatalytic performance of the BIT-Nd and BIT hierarchical microspheres for RhB degradation. (a) Relative variations of RhB concentration over time ($C_0 = 10$ mg L^{-1}) under different degradation conditions in the presence of BIT-Nd and (b) the corresponding $\ln(C/C_0) - t$ plots with the calculated k and R^2 values. (c) Piezo-photocatalytic activity of BIT-Nd for degrading the RhB solution with different initial concentrations. (d) Piezo-photocatalytic activity of BIT-Nd for degrading the RhB solution ($C_0 = 40$ mg L^{-1}) at different stirring speeds. (e) Comparison of the k values between BIT and BIT-Nd for the degradation of RhB solution ($C_0 = 10$ mg L^{-1}) under different conditions. (f) The k values achieved in this work and recently reported piezo-photocatalysis studies.

91.9% and 97.3% were achieved within 15 minutes under the conditions of "Stir200 + light" and "ultrasonic + dark", respectively. Moreover, combining the effect of light and ultrasonic excitations remarkably enhanced the degradation of RhB solution, reaching 97.5% within 8 minutes. The trend of the kinetic curve is consistent with linear fitting kinetic curve trends,[39,40] and the resulting k and R^2 values are summarized in Fig. 4(b). Compared to photocatalysis alone ($k = 0.142$ min^{-1}) and piezocatalysis alone ($k = 0.227$ min^{-1}), the k value achieved by the combined piezo-photocatalysis ($k = 0.407$ min^{-1}) surpasses the sum of the k values for the above two individual catalytic process, as shown in Fig. 4(b). This enhancement is the result of the piezo-phototronic coupling effect, where the piezoelectric field facilitates the separation of carriers and enhances the piezo-photocatalytic performance.[33] Further discussion on the insight mechanisms behind photocatalysis and piezo-photocatalysis will be provided later.

Fig. 4(c) gives the comparison of piezo-photocatalytic performance of BIT-Nd at different initial concentrations of the RhB solution. With an increase in the dye concentration, the degradation rate decreases due to the limited active sites on the surface of the catalyst, which are insufficient for degrading high-concentration dyes. Furthermore, ultrasonic waves are rarely found in natural water systems, and therefore,

piezocatalysis driven by the low-frequency water flow has long been pursued. In order to evaluate the piezo-photocatalytic activity of BIT-Nd driven by the low-frequency water flow, the catalytic performance of BIT-Nd for degrading high-concentration RhB solutions (C_0 = 40 mg L^{-1}) under the conditions of light and stirring with different stirring speeds was measured, as shown in Fig. 4(d). Under light illumination, as the stirring speed increased from 200 to 1000 rpm, the time required for degrading 95% RhB decreased from 40 to 30 minutes. This degradation rate is comparable to the recently reported degradation rates of other piezo-photocatalysts under ultrasonication and illumination,[18,39,41,42] indicating the great potential of the BIT-Nd hierarchical microspheres for future low-frequency piezocatalysis applications.

Furthermore, we compared the catalytic activity of BIT-Nd and BIT for the degradation of RhB solution (C_0 = 10 mg L^{-1}) under different conditions. The reduction of RhB concentration over time and the calculated k value are summarized in Fig. S5† and 4(e), respectively. BIT-Nd presents a higher piezocatalytic degradation efficiency with a k value of 0.227 min^{-1}, 9.5 times higher than that of BIT, indicating the superior piezocatalytic capability of BIT-Nd. Furthermore, when exposed to light (190–1100 nm) or visible light (420–1100 nm) irradiation alone, better photocatalytic activity of BIT-Nd than that of BIT can be obtained, which is attributed to its narrower band gap, higher light absorption and faster charge transfer. These factors contributed to the generation of more photoinduced electron–hole pairs and a reduced recombination rate of carriers. Moreover, the degradation efficiency is apparently enhanced by combining ultrasonication and light irradiation for both the BIT and BIT-Nd powders. To assess the durability and stability of BIT and BIT-Nd powders, 5 cycles for repeatable piezo-photocatalysis are shown in Fig. S6.† The slight decrease in the degradation rate after 5 cycles exhibits a stable recycling ability of BIT-Nd and BIT powders. For the high-concentration RhB solution (C_0 = 40 mg L^{-1}), the piezo-photocatalytic degradation efficiency reached 92.5% within 16 min in the presence of BIT-Nd, which was faster than that of BIT, as shown in Fig. S7.† Fig. 4(f) shows a comprehensive comparison of k values from the recent reports and this work, and the catalytic conditions are summarized in Table S1,† where the catalytic performance of BIT-Nd is highly promising as a coupled piezo-photocatalyst.

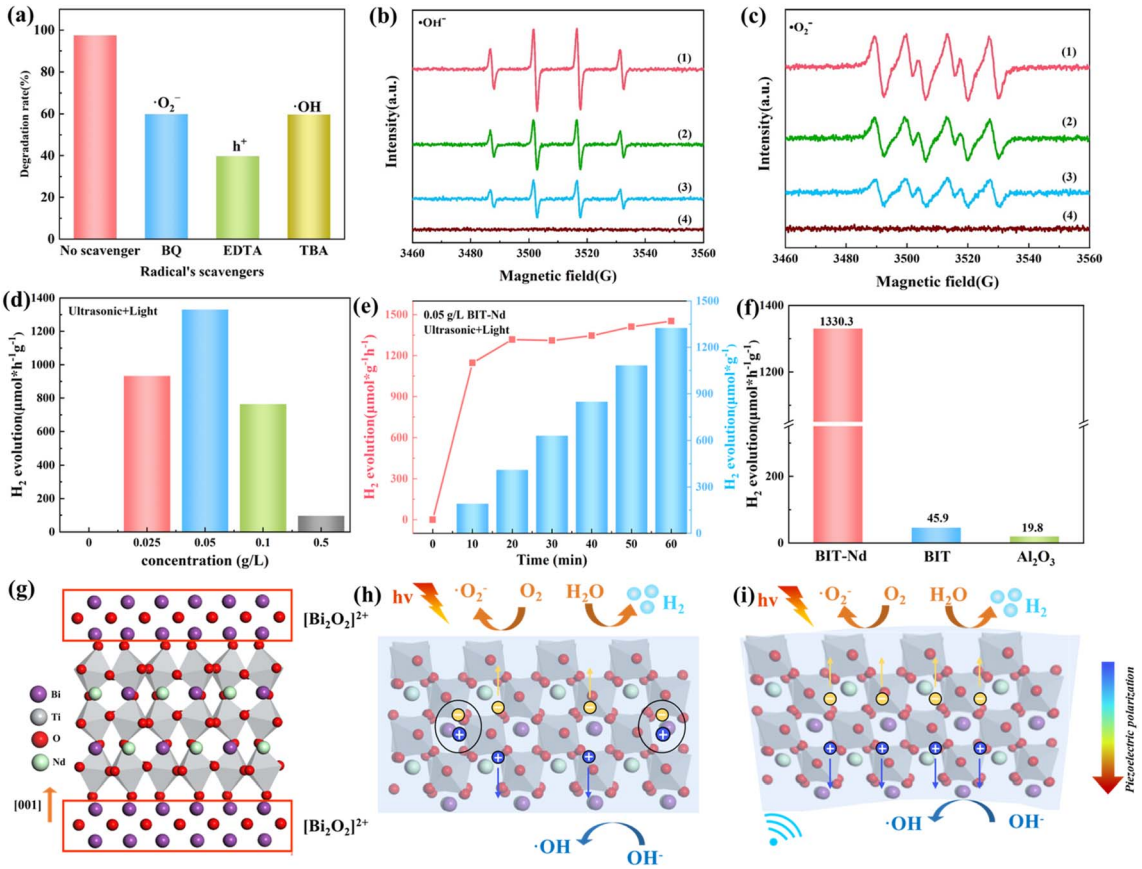

Fig. 5 (a) Under ultrasonic conditions and light excitation, the degradation rate of RhB solution (C_0 = 10 mg L^{-1}) in the presence of BIT-Nd and different scavengers. ESR spectra of (b) DMPO-·OH and (c) DMPO/DMSO-$\cdot O_2^-$ measured during the piezo-photocatalysis (1, ultrasonic + light), piezocatalysis (2, ultrasonic + dark), and photocatalysis (3, Stir200 + light) processes in the presence of BIT-Nd, as well as the piezo-photocatalysis process (4, ultrasonic + light) in the absence of any catalyst. (d) Under ultrasonic conditions and light excitation, the H_2 production rates at different contents of BIT-Nd. (e) The amount of H_2 over time during the piezo-photocatalysis process (ultrasonic + light) in the presence of 0.05 g L^{-1} BIT-Nd. (f) The calculated H_2 production rates of 0.05 g L^{-1} BIT-Nd, BIT, and Al_2O_3. (g) Crystal structure of BIT-Nd. Proposed mechanisms for the (h) photocatalysis and (i) piezo-photocatalysis processes.

In order to investigate the generated active species in the process of piezo-photocatalytic degradation of RhB solution (C_0 = 10 mg L^{-1}), phenylhydrazine (BQ), ethylenediamine tetraacetate dehydrate (EDTA), and *tert*-butyl alcohol (TBA) were used to remove the superoxide ($\cdot O_2^-$), holes (h^+), and hydroxyl ions ($\cdot$OH), respectively. As shown in Fig. 5(a), under ultrasonic conditions and light irradiation, the addition of BQ, TBA, and EDTA greatly reduced the decomposition rate of RhB from 97.5% (no additive) to 59.9%, 59.7%, and 39.7%, respectively. The results imply that h^+ acts as a major free radical during the degradation process and the active oxygen species $\cdot O_2^-$ and $\cdot$OH play important roles during the catalytic oxidation process. In addition, the $\cdot$OH and $\cdot O_2^-$ radical species produced during the photocatalysis, piezocatalysis, and piezo-photocatalysis processes were detected by the electron spin resonance (ESR) method,[43] as shown in Fig. 5(b) and (c). The strongest radical signal is detected under the combined conditions of ultrasound and light irradiation, indicating that this state produces relatively higher amounts of active species. This is consistent with the result of the dye degradation mentioned above (Fig. 4(a) and (b)), and further confirms that piezoelectric polarization promotes the photocatalytic performance of BIT-Nd. Based on the above discussion, the possible reaction process can be explained by the following steps:

$$\mathrm{BIT-Nd} \xrightarrow{\text{light+ultrasound}} \mathrm{BIT-Nd} + h^+ + e^- \quad (1)$$

$$O_2 + e^- \rightarrow \cdot O_2^- \quad (2)$$

$$OH^- + h^+ \rightarrow \cdot OH \quad (3)$$

$$\cdot OH + \cdot O_2^- + h^+ + \text{dye molecules} \rightarrow CO_2 + H_2O \quad (4)$$

Since the BIT-Nd hierarchical microspheres exhibited an excellent degradation rate for the RhB aqueous solution, the catalytic performance of BIT-Nd was further assessed by the water splitting for H_2 production in pure water, without the addition of cocatalysts and scavengers. Under ultrasonic conditions and light excitation, the yield of H_2 increased with increasing BIT-Nd content, when the content of the BIT-Nd is low (<0.05 g L^{-1}). However, when the content of BIT-Nd exceeded 0.05 g L^{-1} and continued to increase, the production rate of H_2 did not further improve due to catalyst aggregation.[44] The highest H_2 yield (1330.3 μmol g^{-1} h^{-1}) was achieved when the BIT-Nd content was 0.05 g L^{-1}, indicating an optimized content for high catalytic performance, as illustrated in Fig. 5(d). Fig. 5(e) shows that the production of H_2 by BIT-Nd steadily increased over 60 minutes under ultrasonic conditions and light excitation. And the XRD pattern of BIT-Nd powders after six cycles of H_2 production is shown in Fig. S8.† The characteristic peaks of BIT-Nd before and after the reaction are almost consistent, indicating the high stability of BIT-Nd powders. As shown in Fig. 5(f), the non-ferroelectric sample Al_2O_3 was tested to evaluate whether the H_2 production was caused by sonocatalysis. Negligible H_2 production was observed under the same conditions. For comparison, the piezo-photocatalytic activity of BIT for H_2 production was also measured under the same conditions, where a H_2 production rate (45.9 μmol g^{-1} h^{-1}) was obtained. Table 1 summarizes the H_2 production performance achieved in this work and previous reports with that of many other piezo-photocatalysts. The results highlight the promising catalytic activity of BIT-Nd as a coupled piezo-photocatalyst in H_2 generation, even in pure water, demonstrating its comparable performance to these systems with the addition of sacrificial agents.

Fig. 5(g) displays the layered perovskite structure of BIT-Nd, composed of the bismuth oxide and perovskite-like layers stacked alternately along the *c* axis. The schematic diagrams illustrating the charge transfer behaviors in the photocatalysis and piezo-photocatlysis processes are shown in Fig. 5(h) and (i), respectively. For the photocatalysis, a large number of photo-induced electron–hole pairs are generated through photo-emission. However, the high recombination rate of electron–hole pairs limits their participation in the redox reaction at the surface of BIT-Nd, leading to a low photocatalytic performance in this state,[45–48] as shown in Fig. 5(h). When the system is subjected to periodic mechanical stress and light, as shown in Fig. 5(i), the [TiO_6] octahedron deforms and forms an internal electric field to promote the electron and hole transport in opposite directions. The introduction of piezoelectric polarization enables efficient charge separation and inhibits the recombination of photoinduced charges. Compared to BIT, the

Table 1 Comprehensive comparison of previously reported piezo-photocatalysts and this work for H_2 evolution

	Catalyst	Electrolyte	Sacrificial agents	Conditions	H_2 evolution (μmol g^{-1} h^{-1})	Ref.
1	Pt/Bi_4NbO_8Br nanoplates	H_2O	Lactic acid	Ultrasonic: 40 kHz, 280 W; light: Visible light 300 W	380	46
2	$Bi_4Ti_{2.8}Cr_{0.1}$ $Nb_{0.1}O_{12}$/5%-g-C_3N_4	H_2O	Na_2S	Ultrasonic: 45 kHz; light: 300 W	696	18
3	$Na_{0.5}Bi_{0.5}TiO_3$	H_2O	Triethanolamine	Ultrasonic: 40 kHz, 110 W; light: 200 mW cm^{-2}	158	49
4	$(Na_{0.5}Bi_{0.5})TiO_3$–$Ba(Ti_{0.5}Ni_{0.5})O_3$	H_2O	Triethanolamine	Ultrasonic: 40 kHz, 200 W; light: 300 W	450	50
5	$PbTiO_3$/CdS	H_2O	Na_2S and Na_2SO_3	Ultrasonic: 40 kHz, 100 W; light: 300 W	849	51
6	$KNbO_3/MoS_2$	H_2O	Triethanolamine	Ultrasonic: 40 kHz, 100 W; light: 300 W	96	52
7	$Au/AgNbO_3$	H_2O	$FeSO_4$	Ultrasonic: 40 kHz, 110 W; light: Visible light 300 W	392	53
8	$PtRu/C_3N_5$	H_2O	Triethanolamine	Ultrasonic: 40 kHz, 120 W; light: 100 W	1010	54
10	d-FCNs	H_2O	Na_2SO_3	Ultrasonic: 40 kHz; light: visible light	638.74	55
11	BIT-Nd	H_2O	—	Ultrasonic: 45 kHz, 200 W; light: 300 W	1330.3	This work

enhanced spectral absorption, larger piezoelectric potential under pressure, and faster charge transfer enable the BIT-Nd hierarchical microspheres to show a more excellent piezo-photocatalytic activity for efficient pollutant degradation and H_2 production.

3. Conclusions

This paper presents a detailed evaluation of the piezo-photocatalytic properties of the $Bi_{3.15}Nd_{0.85}Ti_3O_{12}$ (BIT-Nd) nanosheet-assembled microspheres for high-efficiency hydrogen production and dye degradation for the first time. Due to the built-in electric field promoting the electron–hole pair separation, the H_2 evolution rate of BIT-Nd reached 1330.3 μmol g^{-1} h^{-1} under ultrasonic conditions and light excitation without any cocatalyst and scavenger. Furthermore, in the process of degrading a 100 mL RhB solution with an initial concentration of 10 mg L^{-1}, the piezo-photocatalytic process achieved a remarkable removal efficiency of 97.5% within 8 minutes, leading to an ultrahigh k value of 0.407 min^{-1}, which surpasses the sum of the k values for the photocatalysis and piezocatalysis alone. The evaluation combines theoretical calculations with experimental results, which collectively reveal the positive effects of Nd^{3+} doping on improving the piezoelectric properties of BIT through lattice distortion and the reduction of the band gap *via* band structure engineering. At the same time, the thinner BIT-Nd nanosheets were easier to deform under the external forces and then produced higher piezoelectric fields. The hierarchical microspheres, higher piezoelectric potential, and efficient spectral absorption of the BIT-Nd nanosheet-assembled microspheres consistently determine the ultra-high piezo-photocatalytic performance. The lattice distortion and band structure engineering provide new insights for designing excellent piezo-photocatalysts.

4. Experimental

4.1 Chemicals and reagents

All chemicals and reagents were obtained commercially and used in the study without further purification, including analytical grade Bi_2O_3 (99.9%, Macklin), Nd_2O_3 (99.99%, Aladdin), TiO_2 (99.0%, Macklin), tetrabutyl titanate (99.0%, Adamas), $Bi(NO_3)_3 \cdot 5H_2O$ (≥99.0%, Aladdin), $Nd(NO_3)_3 \cdot 6H_2O$ (99.0%, Macklin), and NaOH (≥98%, pellets, Macklin).

4.2 Synthesis of BIT and BIT-Nd hierarchical microspheres

$Bi_{3.15}Nd_{0.85}Ti_3O_{12}$ (BIT-Nd) and $Bi_4Ti_3O_{12}$ (BIT) hierarchical microspheres were synthesized by a hydrothermal synthesis method. A certain amount of $Bi(NO_3)_3 \cdot 5H_2O$, and $Nd(NO_3)_3 \cdot 6H_2O$ was added to the 6 mL tetrabutyl titanate solution with a Bi : Nd : Ti molar ratio of 3.15 : 0.85 : 3. Subsequently, a 70 mL NaOH solution with a concentration of 3 M was added to the above prepared precursor solution. The mixture was then continuously stirred magnetically for 0.5 h followed by transferring it into a 100 mL Teflon-lined stainless autoclave and heating at 200 °C for 24 h. The collected powders were filtered and washed with deionized water and ethanol at least three times and dried at 80 °C in air for 6 h to obtain the BIT-Nd hierarchical microspheres. BIT hierarchical microspheres were synthesized with a Bi : Ti molar ratio of 4 : 3 under the same synthesis conditions.

4.3 Characterization

The phase structures of the BIT-Nd and BIT hierarchical microspheres were evaluated by the X-ray diffraction technique (XRD, PAN-analytical Empyrean, Netherlands). The morphology was observed by scanning electron microscopy (SEM, Ultim Max 40, Tescan mira4 LMH), and energy dispersive spectroscopy (EDS) was used to characterize the element distribution. The nanostructures were observed by high-resolution transmission electron microscopy (HR-TEM, Titan G2 60–300, USA). The specific surface area was analyzed by the Brunauer–Emmett–Teller (BET, ASAP 2460, USA) method. X-ray photoelectron spectroscopy (XPS, ESCALAB 250Xi, USA) was carried out with standard Al Kα 1 excitation. The piezoelectric properties were evaluated by the contact mode piezo-response force microscopy (PFM, NanoMan VS, USA) characterization. The UV-vis absorbance spectra were obtained *via* a UV-vis spectrometer (UV-2000i and UV-2450, Shimadzu, Japan).

Electrochemical impedance spectroscopy (EIS), photocurrent measurement and Mott–Schottky curve measurements were performed using a standard three-electrode electrochemical workstation (CHI604E, China). The experimental setup comprised a three-electrode system, with a 0.5 M Na_2SO_4 solution serving as the electrolyte. The counter and reference electrodes employed were the Pt electrode and Ag/AgCl electrode, respectively, both immersed in a 0.5 M Na_2SO_4 solution. To prepare the working electrode, 20 mg of the catalyst was dispersed in a mixture of 50 μL of Nafion aqueous solution and 2 mL of ethylene glycol. The homogenized suspension was then coated onto a conductive fluorine-doped tin oxide glass substrate. For EIS measurements, a frequency range of 0.05 to 100 kHz was used. Photocurrent measurements were conducted on the working electrode, illuminated by a 300 W xenon lamp. The Mott–Schottky curves for the working electrode were obtained at frequencies of 1 kHz, 2 kHz, and 3 kHz.

For the ESR test, take a 5 mL glass bottle and add 1 mL of powder aqueous solution (for ·OH) or DMSO solution (for $\cdot O_2^-$). Quickly extract 50 μL of solution and sonicate or illuminate for 15 minutes. Mix this extraction solution and 5 μL DMPO thoroughly in a centrifuge tube. Then, use a capillary tube to extract the mixed solution and seal the bottom with plasticine. Make sure the surface is clean and place it in a glass tube for ESR testing on a Bruker model A300 spectrometer (Bruker A300, Germany).

4.4 Catalytic activity evaluation for hydrogen production

The piezo-, photo-, and piezo-photocatalytic performances of the BIT-Nd hierarchical microspheres for hydrogen production were measured. Different doses of the BIT-Nd powders were added to 70 mL of deionized (DI) water. A xenon lamp (300 W, PLS-SXE300E, Beijing Perfect Light) and ultrasonic machine

(200 W, 45/80/100 kHz, KD-200, China) were used to provide a periodic mechanical load and simulated solar source, respectively. The amounts of generated H_2 were measured by gas chromatography (Fanwei GC-6600, China) using ultra-pure N_2 (99.9995 vol%) as the carrier gas and a thermal conductivity detector.

4.5 Catalytic activity evaluation for pollutant degradation

100 mg of the BIT-Nd and BIT powders were placed in 100 mL of RhB aqueous solution with different initial concentrations (C_0 = 10 mg L^{-1}, 20 mg L^{-1}, and 30 mg L^{-1}). The mixture was stirred for 30 minutes in the dark to achieve adsorption–desorption equilibrium between the dye and catalyst. The relative variations of RhB concentration over time in the photocatalytic, piezocatalytic and piezo-photocatalytic processes were evaluated, respectively. Specifically, the process of photocatalysis required a low stirring speed of 200 rpm to ensure that the active sites of powders were exposed to light, referred to "Stir200 + light". For comparison, and as a control, the degradation ratio (D%) and the first-order kinetic rate constant (k) were calculated according to the following eqn (5) and (6):

$$\text{Degradation rate } (D\%) = [1 - (C/C_0)] \times 100\% \quad (5)$$

$$\ln(C/C_0) = kt \quad (6)$$

where t is the reaction time, C and C_0 are the instantaneous and original dye concentrations, respectively, and k can be obtained from the slope of the $\ln(C_0/C) - t$ curve to determine the kinetics of the degradation process.

4.6 Finite element analysis

COMSOL Multiphysics® (combinations of solid mechanics, electrostatics, and electrical circuit modules) was used to set up a 3D finite-element model to analyze the piezoelectric potential.

4.7 DFT calculations

The density functional theory (DFT) was based on the utilization of the Cambridge sequential total energy package (CASTEP) in Material Studio software. The Perdew–Burke–Ernzerh (PBE) generalized gradient approximation (GGA) was chosen for exchange–correlation potential. The convergence tolerances of the energy, the maximum force and displacement were set as 1×10^{-5} eV, 0.03 eV $Å^{-1}$ and 0.001 Å, respectively. A k-point grid of $6 \times 6 \times 1$ was adopted for structure optimizations.

Author contributions

Yan Zhao: conceptualization, methodology, investigation, writing – original draft. Yan Zhang: supervision, conceptualization, writing – review & editing. Qianqian Xu: conceptualization, investigation. Hanyu Gong: data curation. Mingyang Yan: formal analysis. Kaiyu Feng: investigation. Xiang Zhou: software. Xuefan Zhou: conceptualization, writing – review & editing. Dou Zhang: conceptualization, supervision.

Conflicts of interest

The authors declare that they have no known competing financial interests or personal relationships that could have appeared to influence the work reported in this paper.

Acknowledgements

This work was supported by the National Key Research and Development Program (2022YFB3807404), the National Natural Science Foundation of China (No. 52302158), the Overseas Talent Introduction Project of China,the Hundred Youth Talents Program of Hunan and the State Key Laboratory of Powder Metallurgy, Central South University, Changsha, China.

References

1 L. Chen, X. Dai, X. Li, J. Wang, H. Chen, X. Hu, H. Lin, Y. He, Y. Wu and M. Fan, *J. Mater. Chem. A*, 2021, **9**, 13344–13354.
2 Q. Liu, Q. Hu, D. Zhai, Q. Sun, H. Luo and D. Zhang, *J. Mater. Chem. A*, 2021, **9**, 17841–17854.
3 Q. Liu, F. Zhan, H. Luo, D. Zhai, Z. Xiao, Q. Sun, Q. Yi, Y. Yang and D. Zhang, *Appl. Catal., B*, 2022, **318**, 121817–121831.
4 W. Feng, J. Yuan, F. Gao, B. Weng, W. Hu, Y. Lei, X. Huang, L. Yang, J. Shen, D. Xu, X. Zhang, P. Liu and S. Zhang, *Nano Energy*, 2020, **75**, 104990–105001.
5 Y. Luo, L. Tang, U. Khan, Q. Yu, H.-M. Cheng, X. Zou and B. Liu, *Nat. Commun.*, 2019, **10**, 269–278.
6 Q. Liu, F. Zhan, H. Luo, X. Luo, Q. Yi, Q. Sun, Z. Xiao, Y. Zhang, D. Zhang and C. R. R. Bowen, *Adv. Funct. Mater.*, 2023, 230376–230391.
7 W. Liu, P. Wang, Y. Ao, J. Chen, X. Gao, B. Jia and T. Ma, *Adv. Mater.*, 2022, **34**, 2202508–2202516.
8 L. Pan, S. Sun, Y. Chen, P. Wang, J. Wang, X. Zhang, J. J. Zou and Z. L. Wang, *Adv. Energy Mater.*, 2020, **10**, 2000214–2000239.
9 Z. Liu, B. Wang, D. Chu and C. Cazorla, *J. Mater. Chem. A*, 2022, **10**, 18132–18146.
10 K. Wang, D. Shao, L. Zhang, Y. Zhou, H. Wang and W. Wang, *J. Mater. Chem. A*, 2019, **7**, 20383–20389.
11 X. Xue, W. Zang, P. Deng, Q. Wang, L. Xing, Y. Zhang and Z. L. Wang, *Nano Energy*, 2015, **13**, 414–422.
12 X. Liu, L. Xiao, Y. Zhang and H. Sun, *J. Materiomics*, 2020, **6**, 256–262.
13 R. Tang, D. Gong, Y. Zhou, Y. Deng, C. Feng, S. Xiong, Y. Huang, G. Peng and L. Li, *Appl. Catal., B*, 2022, **303**, 120929–120945.
14 Z. Chen, H. Jiang, W. Jin and C. Shi, *Appl. Catal., B*, 2016, **180**, 698–706.
15 H. Irie, M. Miyayama and T. Kudo, *J. Appl. Phys.*, 2001, **90**, 4089–4094.
16 X. Liu, T. Wang, G. Li, G. Liu, J. Qiu, Z. Guo, H. Hao, J. Dong, H. Liu and J. Xing, *J. Alloys Compd.*, 2023, **936**, 168367–168377.

17 Q. Tang, J. Wu, X.-Z. Chen, R. Sanchis-Gual, A. Veciana, C. Franco, D. Kim, I. Surin, J. Pérez-Ramírez and M. Mattera, *Nano Energy*, 2023, 108202–108212.
18 J. Bai, J. Xiang, C. Chen and C. Guo, *Chem. Eng. J.*, 2023, **456**, 141095–141102.
19 S. Tu, H. Huang, T. Zhang and Y. Zhang, *Appl. Catal., B*, 2017, **219**, 550–562.
20 X. Lin, Q. Guan, C. Zou, T. Liu, Y. Zhang, C. Liu and H. Zhai, *Mater. Sci. Eng. B*, 2013, **178**, 520–526.
21 R. Nie, J. Yuan, Q. Chen, J. Xing, J. Zhu and W. Zhang, *J. Am. Ceram. Soc.*, 2019, **102**, 5432–5442.
22 U. Chon, J. S. Shim and H. M. Jang, *Solid State Commun.*, 2004, **129**, 465–468.
23 U. Chon, H. M. Jang, M. G. Kim and C. H. Chang, *Phys. Rev. Lett.*, 2002, **89**, 087601–087603.
24 X. Xie, Z. Zhou, R. Liang and X. Dong, *J. Materiomics*, 2021, **7**, 59–68.
25 C. Gi Ppeum, C. H. O. Sam Yeon, J. Do Hyun, B. U. Sang Don, L. E. E. Gyoung Ja and L. E. E. Min Ku, *New Phys.: Sae Mulli*, 2015, **65**, 657–663.
26 S. Tu, Y. Guo, Y. Zhang, C. Hu, T. Zhang, T. Ma and H. Huang, *Adv. Funct. Mater.*, 2020, **30**, 2005158–2005189.
27 W. Feng, J. Yuan, L. Zhang, W. Hu, Z. Wu, X. Wang, X. Huang, P. Liu and S. Zhang, *Appl. Catal., B*, 2020, **277**, 119250–119260.
28 T. Patri, T. Durga Rao, K. S. K. R. Chandra Sekhar, S. Raghupathi Rao, S. Rayaprol and P. D. Babu, *Phys. Status Solidi B*, 2022, **259**, 2200223–2200235.
29 X. Ruan, Y. Li, X. Wang and X. Yao, *Ferroelectrics*, 2010, **404**, 119–126.
30 Z. Zhang, Q. Dong, P. Li, S. L. Fereja, J. Guo, Z. Fang, X. Zhang, K. Liu, Z. Chen and W. Chen, *J. Phys. Chem. C*, 2021, **125**, 24814–24822.
31 H. Yu, F. Chen, X. Li, H. Huang, Q. Zhang, S. Su, K. Wang, E. Mao, B. Mei, G. Mul, T. Ma and Y. Zhang, *Nat. Commun.*, 2021, **12**, 4594–4604.
32 X. Zhou, Q. Sun, D. Zhai, G. Xue, H. Luo and D. Zhang, *Nano Energy*, 2021, **84**, 1–12.
33 Z. Xie, X. Tang, J. Shi, Y. Wang, G. Yuan and J.-M. Liu, *Nano Energy*, 2022, **98**, 107247–107258.
34 Q. Liu, F. Zhan, X. Luo, Q. Yi, Z. Xiao, D. Zhai, J. Huang, Y. Zhang, H. Luo, D. Zhang and C. R. Bowen, *Nano Energy*, 2023, **108**, 108252–108266.
35 R. Xu, J. Karthik, A. R. Damodaran and L. W. Martin, *Nat. Commun.*, 2014, **5**, 1–7.
36 P. Mori-Sánchez, A. J. Cohen and W. Yang, *Phys. Rev. Lett.*, 2008, **100**, 146401–146404.
37 H. Xiao, J. Tahir-Kheli and W. A. Goddard III, *J. Phys. Chem. Lett.*, 2011, **2**, 212–217.
38 J. Wu, N. Qin and D. Bao, *Nano Energy*, 2018, **45**, 44–51.
39 H. Zheng, X. Li, K. Zhu, P. Liang, M. Wu, Y. Rao, R. Jian, F. Shi, J. Wang, K. Yan and J. Liu, *Nano Energy*, 2022, **93**, 1–13.
40 Y. Zhao, Q. Xu, X. Zhou, M. Yan, H. Gong, X. Yuan, H. Luo, K. Zhou, D. Zhang and C. Bowen, *Ceram. Int.*, 2023, **49**, 8259–8270.
41 Q. Liu, D. Zhai, Z. Xiao, C. Tang, Q. Sun, C. R. Bowen, H. Luo and D. Zhang, *Nano Energy*, 2022, **92**, 1–14.
42 J. P. Ma, J. Ren, Y. M. Jia, Z. Wu, L. Chen, N. O. Haugen, H. T. Huang and Y. S. Liu, *Nano Energy*, 2019, **62**, 376–383.
43 Q. Liu, F. Zhan, H. Luo, X. Luo, Q. Yi, Q. Sun, Z. Xiao, Y. Zhang, D. Zhang and C. R. Bowen, *Adv. Funct. Mater.*, 2023, **33**, 2303736.
44 Y. Zhang, P. T. T. Phuong, N. P. H. Duy, E. Roake, H. Khanbareh, M. Hopkins, X. Zhou, D. Zhang, K. Zhou and C. Bowen, *Nanoscale Adv.*, 2021, **3**, 1362–1374.
45 S. Y. Lan, C. Yu, F. Sun, Y. X. Chen, D. Y. Chen, W. J. Mai and M. S. Zhu, *Nano Energy*, 2022, **93**, 106792–106803.
46 C. Hu, H. Huang, F. Chen, Y. Zhang, H. Yu and T. Ma, *Adv. Funct. Mater.*, 2020, **30**, 1908168–1908178.
47 X. Zhou, F. Yan, S. Wu, B. Shen, H. Zeng and J. Zhai, *Small*, 2020, **16**, 2001573–2001588.
48 H. You, Z. Wu, L. Zhang, Y. Ying, Y. Liu, L. Fei, X. Chen, Y. Jia, Y. Wang and F. Wang, *Angew. Chem.*, 2019, **131**, 11905–11910.
49 Z. Zhao, L. Wei, S. Li, L. Zhu, Y. Su, Y. Liu, Y. Bu, Y. Lin, W. Liu and Z. Zhang, *J. Mater. Chem. A*, 2020, **8**, 16238–16245.
50 H. Xiao, W. Dong, Q. Zhao, F. Wang and Y. Guo, *J. Hazard. Mater.*, 2021, **416**, 125808–125816.
51 X. Huang, R. Lei, J. Yuan, F. Gao, C. Jiang, W. Feng, J. Zhuang and P. Liu, *Appl. Catal., B*, 2021, **282**, 119586–119596.
52 S. Jia, Y. Su, B. Zhang, Z. Zhao, S. Li, Y. Zhang, P. Li, M. Xu and R. Ren, *Nanoscale*, 2019, **11**, 7690–7700.
53 S. Li, Z. Zhao, M. Liu, X. Liu, W. Huang, S. Sun, Y. Jiang, Y. Liu, J. Zhang and Z. Zhang, *Nano Energy*, 2022, **95**, 107031–107043.
54 S. Shi, Y. Jiang, Y. Yu, M. Liang, Q. Bai, L. Wang, D. Yang, N. Sui and Z. Zhu, *Adv. Funct. Mater.*, 2023, **33**, 2210850–2210866.
55 Y. Wang, Y. Guo, C. Zeng, D. Yang, Y. Zhang, L. Wu, Y. Wu, J. Hao, J. Wang and R. Yang, *Nano Energy*, 2022, **104**, 107983–110792.